NANO LETTERS

2008
Vol. 8, No. 8
2485-2489

Cracks in Magnetic Nanocrystal Films: Do Directional and Isotropic Crack Patterns Follow the Same Scaling Law?

Anh Tu Ngo, Johannes Richardi, and Marie Paule Pileni*

Laboratoire des Matériaux Mésoscopiques et Nanométriques (LM2N), UMR CNRS 7070, Université Pierre et Marie Curie, bât F, BP 52, 4 Place Jussieu, 75252 Paris Cedex 05, France

Received May 26, 2008; Revised Manuscript Received June 27, 2008

ABSTRACT

In this letter, we show that the use of nanocrystals enables new insights into the scaling law of crack patterns. Directional and isotropic crack patterns made of γ-Fe_2O_3 nanocrystals follow the same scaling law, with the film height varying by 3 orders of magnitude. A simple two-dimensional computer model for elastic fracture also leads to the same scaling behavior for directional and isotropic cracks, in good agreement with the experiments.

Cracks due to a shrinking film restricted by adhesion to a surface have been studied over several decades. The similarities between the geometries of the different patterns are observed over a wide range of scales,[1–6] from millimeters to kilometers. This suggests a universal mechanism. Different morphologies of crack patterns, such as isotropic, directional, radial, ring, spiral, and others can be observed, depending on the drying process of a colloidal suspension.[7–11] Recent experiments[1,11] have shown that the areas and distances between cracks increase with film height. However, different scaling laws were, surprisingly, observed for directional (1D) and isotropic (2D) cracks.[1,11] Thus, Allain and Limat[1] observed a deviation from linear scaling of the average crack distance with height, h, in their directional drying experiments, in good agreement with a theoretical model developed by Komatsu and Sasa[12] which predicted that the distance between cracks varied as $h^{2/3}$. This is different from the linear relationship between the square root of the area and the height found by Groisman and Kaplan[11] and theoretically confirmed by Leung and Néda[13] for the isotropic crack patterns. To account for these differences, the scaling behavior of directional (1D and 2D) and isotropic (2D) crack patterns are here directly compared in the maghemite nanoparticle films over 3 orders of magnitude. Furthermore, a new method to orient the cracks is employed by applying a magnetic field to the film during the drying process. Simulations of 1D and 2D crack formation are theoretically studied using a recently developed model[13] to compare them with those observed in the experiments.

The formation of crack patterns is obtained by injecting 10 nm γ-Fe_2O_3 nanocrystals dispersed either in water (2D cracks) or chloroform (1D and 2D cracks) above a silicon wafer placed at the bottom of a glass beaker. The change in the solvent in which the nanocrystals are dispersed requires a change in the coating agent (Supporting Information). The beaker is covered with a glass plate to reduce the evaporation rate. The evaporation of the solvent occurs at room temperature. During this process, the solution is subjected or not to an applied magnetic field (0.2 T) parallel to the substrate. As the solvent evaporates, the concentration of the solution increases with formation of a gel that adheres to the silicon wafer. Further evaporation induces shrinkage of the thin film layer due to large stresses, but the adhesion to the silicon substrate limits the contraction of the film. This results in large stresses which are at the origin of the crack formation. The crack patterns spanning the whole substrate appear after drying. They are visualized with a scanning electron microscope (SEM) and a digital camera. The layer height (from micrometer to millimeter) and the size of the crack patterns (from micrometer to centimeter) are controlled by the nanocrystal concentrations (Supporting Information). In the case of crack formation in an external applied field, the nanocrystals are dispersed in chloroform, since it allows obtaining a uniform film over all the substrate due to its density being higher than that of water.

We first follow the formation of directional crack patterns for the thickest sample, $h = 415 \pm 5$ μm, by taking photographs at different times using a digital camera (see Figure 1a−d). Figure 1a shows the formation of the first crack in the direction of the applied field, at the middle of

* To whom correspondence should be addressed. E-mail: pileni@sri.jussieu.fr.

10.1021/nl801501y CCC: $40.75
Published on Web 07/16/2008

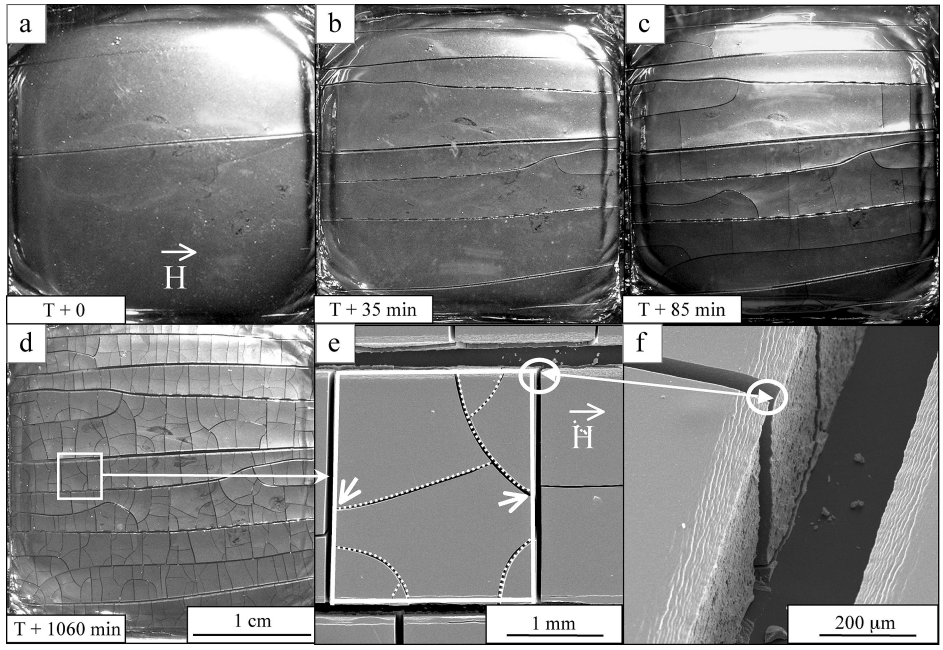

Figure 1. Photographs (a−d) and SEM (e, f) images of directional (1D−2D) crack patterns made of 10 nm γ-Fe_2O_3 nanocrystals produced by applying a magnetic field (0.2 T) during the evaporation process with an average layer height of 415 ± 5 μm. Parts a−d give photographs of the formation of centimeter-size directional cracks (solution volume 5 mL, concentration 28% by weight before drying): (a) formation of the first crack in the direction of the applied field, at the middle of the substrate; (b) successive domain divisions occurring mainly parallel to the applied field leading to equally spaced linear cracks obtained after 35 min of the formation of the first crack; (c, d) formation of perpendicular cracks (c) and final crack patterns (d) obtained after 85 and 1060 min of the formation of the first crack, respectively. (e, f) SEM images at zero angle (e) of a primary 2D crack (solid lines) with secondary 2D cracks (dashed lines) and 45° tilt (f).

the magnetic gel where the stress in the fragment is the largest.[14] Successive domain divisions occur, mainly parallel to the applied field, leading to equally spaced linear cracks (see Figure 1b). About 85 min after the formation of the first crack, cracks perpendicular to the directional ones appear and invade all the sample as the evaporation continues (Figure 1c). Further evaporation induces new cracks which appear inside each fragment bounded by cracks parallel and perpendicular to the direction of the applied magnetic field (Figure 1d,e). The formation of directional cracks produced by applying a magnetic field parallel to the substrate is explained as follows. In the liquid state, the nanocrystals are free to rotate and their magnetic moments are aligned along the applied magnetic field direction.[15] This favors the attractions between nanocrystals in the direction parallel to the applied field, whereas repulsions take place in the perpendicular direction, leading to a biaxial stress within the film. Therefore, the stress, σ_{yy}, perpendicular to the applied field is larger than that, σ_{xx}, parallel to the field according to the equation[16]

$$\sigma_{yy} - \sigma_{xx} = \mu_0(H^2 + MH) > 0 \qquad (1)$$

where μ_0, M, and H are the magnetic permeability of the vacuum, the magnetization of the film, and the field, respectively.

The higher stress σ_{yy} is relieved first, leading to the parallel cracks shown in Figure 1a,b. Later on, the stress parallel to the direction of the field will also be relieved, inducing the formation of perpendicular cracks (Figure 1c).

To analyze the experimental data quantitatively, we need to define primary 1D and 2D cracks and secondary 2D cracks. The straight cracks parallel to the direction of the applied field correspond to the first generation of cracks and are called primary 1D cracks. The fragments bounded by these primary 1D cracks and the perpendicular ones (second generation of cracks) are called primary 2D cracks. A magnification of a region in Figure 1d by using SEM shows that a typical primary 2D crack fragment delimited by solid lines (Figure 1e) is four-sided with 90° angles. The mean crack aperture of parallel cracks (first generation of primary 1D cracks) is about twice as large as that of the perpendicular ones (second generation of cracks) and is clearly seen in Figure 1e. At the end of the drying process, the crack patterns (Figure 1e) show that the primary 2D crack fragments are broken into smaller ones (from two to eight domains) corresponding to the third and later generations of cracks, as indicated by the dashed lines in Figure 1e. These new generations of cracks, called secondary 2D cracks, tend to appear at the middle of the sides of existing fragments bounded by primary cracks (see arrows in Figure 1e), which is consistent with the theoretical model of Hornig.[14] It has been checked, by tilting the sample by 45°, that all primary and secondary cracks go straight from the top to the bottom of the film. Figure 1f shows how a typical primary 2D crack goes all the way through the film layer.

The formation of isotropic 2D crack patterns obtained without a magnetic field is shown in Figure 2a−d. Figure 2a shows the formation of a first crack (dashed lines), which splits the magnetic film into two regions. After 7 min, a second crack appears and meets the first orthogonally (solid line in Figure 2b). Then, new cracks form and meet the two

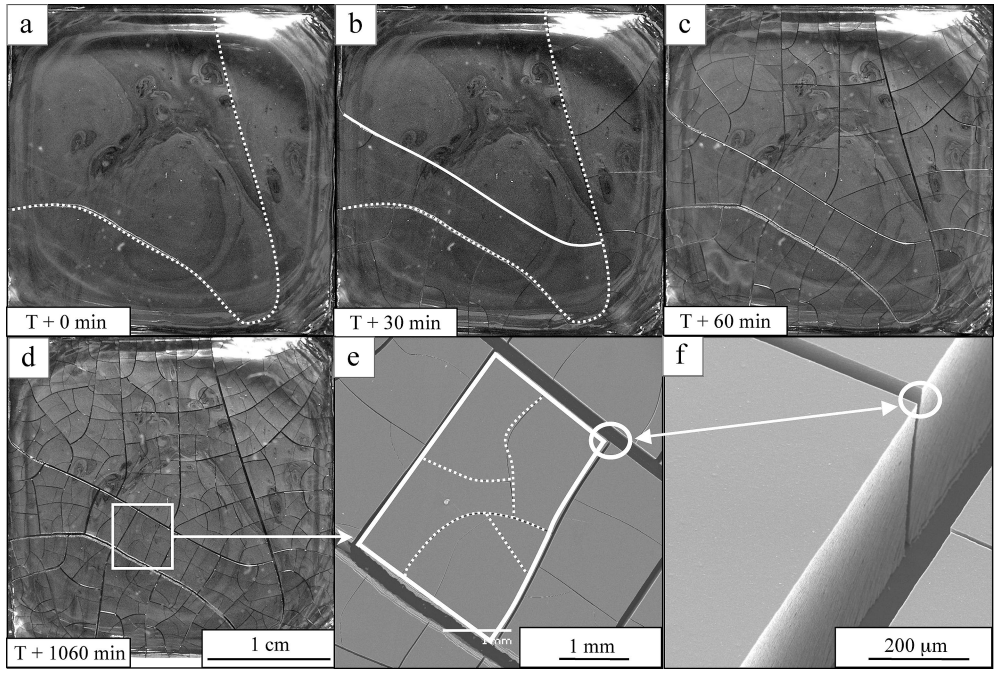

Figure 2. Photographs (a−d) and SEM (e, f) images of isotropic 2D crack patterns made of 10 nm γ-Fe_2O_3 nanocrystals produced without a magnetic field during the evaporation process with an average layer height of 415 ± 5 μm. Parts a−d give photographs of the formation of centimeter-sized isotropic cracks (solution volume 5 mL, concentration 28% by weight before drying): (a) formation of a first crack, which splits the magnetic film into two regions; (b, c) later appearance of a second crack, which meets the first orthogonally, and then formation of new cracks, which meet the two first cracks, usually with junction angles of 90°: (d) isotropic crack patterns obtained at the end of the drying process (d). (e, f) SEM images at zero angle (e) of a primary isotropic 2D crack (solid lines) with secondary 2D cracks (dashed lines) and 45° tilt (f).

first cracks, usually with junction angles of 90° (Figure 2b,c). Finally, isotropic fragments bounded by cracks invade all the sample (Figure 2d). As already observed for other experimental systems,[2,11] the distribution of crack junction angles is peaked at 90° and the fragments bounded by cracks are mainly four-sided with six neighbors.[17] As for the directional crack patterns, a magnification of a region in Figure 2d shows that a typical primary 2D crack fragment delimited by solid lines (Figure 2e) is broken into smaller ones (dashed lines). Again, by tilting the sample, it is clearly shown that a typical crack goes from the top to the bottom of the film (Figure 2f). To analyze the isotropic 2D crack patterns, we use the same criterion as for directional cracks to separate the primary cracks from the secondary ones. Thus, all cracks with an aperture 6 times smaller than those of the two first cracks (Figure 2a,b) are called secondary 2D cracks. A minimum of film height is needed to produce cracks, which is a well-known phenomenon.[18] Only above a film thickness of 2 μm are individual fragments bounded by primary cracks observed. An even larger height ($h > 14\,\mu$m) is necessary to produce secondary cracks. The disappearance of secondary cracks before the primary ones observed by decreasing the film height is explained by the smaller aperture of secondary cracks. Since the secondary cracks do not appear at small heights, we focus our study on the primary crack patterns. This explains the necessity to distinguish between the primary and secondary cracks observed.

We now focus our study on the scaling behavior of 1D and 2D primary crack patterns shown in Figures 1 and 2. The area of the fragments bounded by cracks, A, and the crack distances between regular linear cracks, D, are measured over the whole substrate and their heights, h, by tilting the sample by 45°. The area analysis of the individual fragments of primary 2D cracks, A_{lp} (area of directional 2D cracks) and A_{ip} (area of isotropic 2D cracks), is made by using a public domain image processing and analysis program (NIH Image)[19] over the whole sample on 100 and 600 fragments on average, respectively.

The average crack distance (D), i.e. the average width of strips bounded by primary (1D) cracks, varies from 35 ± 1.5 to 2590 ± 184 μm. The average area square roots of directional 2D and isotropic 2D cracks ($\sqrt{A_{lp}}$, $\sqrt{A_{ip}}$) vary from 18.87 ± 0.49 to 4280 ± 88 μm with the film height (h = 2.83 ± 0.02 to 1000 ± 18 μm).

(i) Let us first consider the directional primary (1D and 2D) cracks to determine the average crack distance (D) and the area square root of directional 2D cracks ($\sqrt{A_{lp}}$) as a function of layer height (h). A linear variation, on a logarithmic scale, of the average crack distance (D) between primary (1D) cracks with the corresponding height (h) is observed (open squares in Figure 3). Using the average experimental value of the dimensionless ratio $K = D/h$ (K = 5.31 ± 0.25), the linear fit gives a slope of 1.00 ± 0.01 in good agreement with the scaling law, $D \approx Kh$. The same linear variation behavior $\sqrt{A_{lp}} = Kh$ is observed, for the average square root area fragments of the primary 2D crack domains defined above and denoted by $\sqrt{A_{lp}}$, with the layer height (see filled triangles in Figure 3). From this, similar dimensionless K values are obtained for 1D and 2D primary cracks.

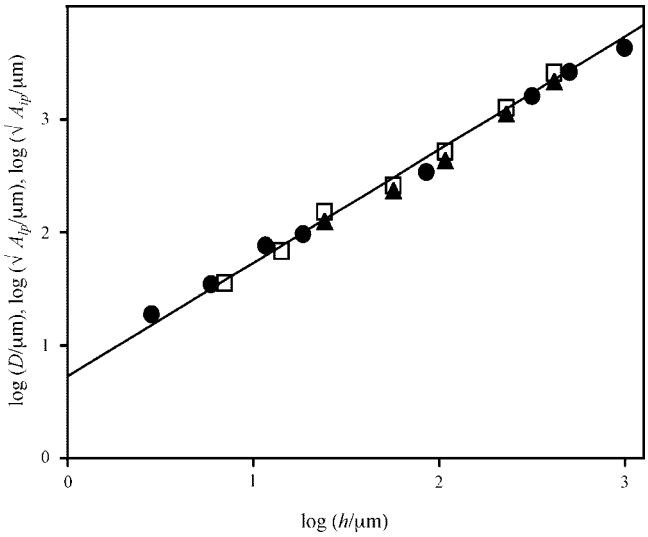

Figure 3. Dependence of the average crack distance (D) and the average square root areas of fragments bounded by primary cracks ($\sqrt{A_{lp}}$, $\sqrt{A_{ip}}$) on the layer height. The average crack distance, D, vs the layer height, h, designated by open squares, fits a linear curve on the logarithmic scale with $\log D = 0.72 + 1.00 \log h$ (solid lines). Solid triangles and circles correspond to the average square root areas of directional and isotropic primary 2D cracks, $\sqrt{A_{lp}}$ and $\sqrt{A_{ip}}$, respectively.

(ii) We now study isotropic 2D primary crack patterns. A linear variation, on a logarithmic scale, of the average square root area of crack domains ($\sqrt{A_{ip}}$) with the layer height is observed (solid circles in Figure 3). Using the average experimental value of the dimensionless ratio $K = \sqrt{A_{ip}}/h$ ($K = 5.42 \pm 0.32$), the linear fit gives a slope of 0.98 ± 0.01, in good agreement with the scaling law, $\sqrt{A_{ip}} \approx Kh$. The scaling law for the isotropic crack patterns is shown over 3 orders of magnitude. The K values obtained for the directional and isotropic cracking systems are equal within experimental error (5.31 ± 0.25 and 5.42 ± 0.32). It is interesting that the same scaling law is found experimentally for directional and isotropic crack patterns. To study the statistical distribution of the size of fragments, we calculated the standard deviation of D/h and A_{ip}/h^2 at the various heights. Within the statistical accuracy error of the experimental approach, the standard deviation does not depend on the height. This shows that also the distribution of the size of fragments follows the linear scaling law with height.

To investigate the universality of the secondary cracks, we carried out a preliminary study on the area fragments, A_{ls} and A_{is}, of the secondary directional and isotropic 2D crack domains. $\sqrt{A_{ls}}$ and $\sqrt{A_{is}}$ follow also a linear scaling as a function of the layer height with a slope of 0.99 ± 0.01. However, the dimensionless ratio K differs by a factor of 2 between the primary cracks ($K = 5.31 \pm 0.25$) and the secondary ones ($K = 2.66 \pm 0.21$). This leads to the linear relationship $\sqrt{A_{ls}} \approx \sqrt{A_{is}} \approx 0.5D$. Hence, the length scale of the pattern for secondary cracks is divided by a factor of 2 compared to the primary cracks; this can be explained by the theoretical model of Hornig,[14] which predicted that cracks tend to appear in the middle of existing fragments (see arrows in Figure 1e); thus, the length scale of the pattern decreases by a factor of 2 with each generation of cracks.

The scaling of directional and isotropic crack patterns with height is now theoretically studied using a recently introduced bundle-spring block model.[13] Simple spring-block models have been widely used to successfully explain experimentally observed crack patterns.[9,13,20,21] In this approach, the layer made of nanocrystals is represented by a large two-dimensional array of blocks where neigbors are connected to each other by coil springs. While in a former work[13] only hexagonal arrays of blocks were used, here hexagonal and square arrays are employed to investigate the influence of the block arrangement on the crack patterns. To study the variation of crack patterns with height, the single springs between blocks[20,21] were replaced by a bundle of h springs with the bundle-spring model.[13] h is a dimensionless number which plays the role of the height. In ref 13, it was shown that, for isotropic crack patterns, the bundle-spring model predicts a linear increase in the square root of the average fragment area bounded by cracks with height, in good agreement with our experiments (solid circles in Figure 3). Here, the bundle-spring model is further developed to answer two questions posed by the experiments:

1. Do the isotropic and directional crack patterns obtained by theory follow the same scaling law as obtained in the experiments?

2. Do the simulations reproduce the anisotropic crack patterns observed by applying a magnetic field?

To answer the first question, at the start of each simulation an initial stress is generated by choosing larger side lengths L_x and L_y than the values L_x^0 and L_y^0 of the relaxed block array. The initial extension of the arrays is defined by the formula $s_x = (L_x - L_x^0)/L_x$ and $s_y = (L_y - L_y^0)/L_y$. For $s_x = s_y = 0.1$, isotropic 2D crack patterns are obtained, in agreement with ref 13. The crack pattern obtained for a square array in Figure 4a shows that the propagation of cracks is markedly influenced by the arrangements of blocks. A uniaxial stress ($s_x = 0.1$ and $s_y = 0$) is used to produce directional cracks. Figure 4b shows the final crack pattern obtained using a square array. The linear cracks are often not continuous, which is explained by an inefficient propagation of the stress built up at the tips of cracks. Isotropic and directional crack patterns were obtained using hexagonal or square arrays in a range of heights between 5 and 50. A detailed explanation of the crack simulation is given in the Supporting Information. To study the scaling laws in the isotropic and directional cases, the average area A of the surface limited by the cracks and the average distance D between the cracks, respectively, are determined. Figure 4c shows a log−log plot of D and $\sqrt{A}$ as a function of h for the directional and isotropic cracks, respectively. All data are well fitted by straight lines with slope 1. For the square array, D (open squares) and $\sqrt{A}$ (solid squares) are identical within the simulation errors at a given height. This is in very good agreement with the experimental behavior observed in Figure 3. However, for the hexagonal array, $\sqrt{A}$ (filled triangles in Figure 4c) is significantly smaller than D (open triangles). This difference is explained by the large number of triangles with a smaller surface area than the four-sided surfaces present in the crack patterns for hexagonal arrays.

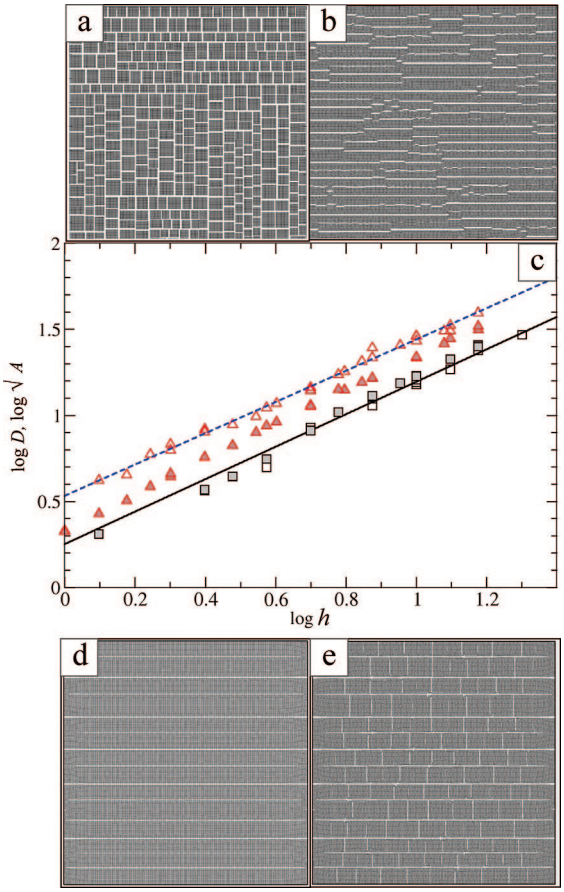

Figure 4. Simulation of isotropic (2D) and linear (1D) cracks: (a, b) crack patterns obtained by simulations for isotropic and uniaxial stress using a square arrangement of blocks ($h = 50$). (c) Scaling of mean separation D and square root area $\sqrt{A}$ of cracks with height. A linear increase $D \sim h$ well describes the data within the statistical accuracy of simulation. Squares and triangles give square and hexagonal arrays with $\log D = 0.25 + 0.94 \log h$ (solid lines) and $\log D = 0.53 + 0.91 \log h$ (dashed lines), respectively. The solid symbols show the square roots of the mean area A for isotropic extension (square (solid squares) and hexagonal (solid triangles) arrays). (d, e) Crack patterns obtained by simulations for biaxial stress ($s_x = 0.50$, $s_y = 0.25$) using a square arrangement of blocks ($h = 50$): (d) patterns after 2 million simulation steps; (e) final result.

Obviously, simulations using the square array better describe the experimental data, in contrast to those obtained using a hexagonal array.

Let us now turn to the second question, whether the simulation can reproduce the anisotropic crack patterns as observed in Figure 1. To answer this question, the dipolar interactions in the film are taken into account by applying a biaxial stress at the beginning of the simulation. A study of the experimental crack patterns obtained at large heights (see Figure 1d) yields the following range of values for the prestrain: $s_x = 0.50-0.60$ and $s_y = 0.25-0.26$. The simulations are carried out using square arrangements of blocks. Figure 4d,e show the time evolution of crack patterns obtained for $s_x = 0.50$ and $s_y = 0.25$ after 2 million and 6 million simulation steps, respectively. During the simulation, the first linear cracks appear perpendicular to the direction where the higher stress is applied (Figure 4d). Then, cracks perpendicular to the first linear ones appear (Figure 4e). This time evolution is in perfect agreement with the experimental formation of primary cracks shown in Figure 1.

In summary, it is shown that directional and isotropic cracks can be produced by applying or not applying an external magnetic field during the drying of a magnetic fluid of γ-Fe_2O_3 nanocrystals. We demonstrated that isotropic (2D) and directional (1D and 2D) primary crack patterns follow the same scaling law over 3 orders of magnitude. To observe these scaling laws, it is very important to distinguish between primary and secondary cracks. The large variation in height in our experiments becomes possible due to the combined use of nanocrystals and electron microscopy. A simple spring-block model reproduces the same scaling for directional and isotropic cracks and explains the formation of directional 2D crack patterns, when a square array of blocks is used. The scaling law, found here, may indicate the universality of crack patterns independent of their dimensions and heights while the disappearance of the secondary cracks at small height is a non universal feature.

Supporting Information Available: Text giving details of the experimental and simulation methods. This material is available free of charge via the Internet at http://pubs.acs.org.

References

(1) Allain, C.; Limat, L. *Phys. Rev. Lett.* **1995**, *74*, 2981–2984.
(2) Shorlin, K. A.; de Bruyn, J. R.; Graham, M.; Morris, S. W. *Phys. Rev. E* **2000**, *61*, 6950–6957.
(3) Dufresne, E. R.; et al. *Phys. Rev. Lett.* **2003**, *91*, 224501–224504.
(4) Pileni, M. P.; Lalatonne, Y.; Ingert, D.; Lisiecki, I.; Courty, A. *Faraday Discuss.* **2004**, *125*, 251–264.
(5) Belousov, V. V.; Gzovsky, M. V. *Phys. Chem. Earth* **1965**, *6*, 409–472.
(6) Heinrich, M.; Gruber, P.; Orso, S.; Handge, U. A.; Spolenak, R. *Nano Lett.* **2006**, *6*, 2026–2030.
(7) Colina, H.; Roux, S. *Eur. Phys. J. E* **2000**, *1*, 189–194.
(8) Xia, Z. C.; Hutchinson, J. W. *J. Mech. Phys. Solids* **2000**, *48*, 1107–1131.
(9) Leung, K. T.; Jozsa, L.; Ravasz, M.; Néda, Z. *Nature* **2001**, *410*, 166.
(10) Nakahara, A.; Matsuo, Y. *Phys. Rev. E* **2006**, *74*, 045102-1–045102-4.
(11) Groisman, A.; Kaplan, E. *Europhys. Lett.* **1994**, *25*, 415–420.
(12) Komatsu, T. S.; Sasa, S. *Jpn. J. Appl. Phys.* **1997**, *36*, 391–395.
(13) Leung, K. T.; Néda, Z. *Phys. Rev. Lett.* **2000**, *85*, 662–665.
(14) Hornig, T.; Sokolov, I.; Blumen, A. *Phys. Rev. E* **1996**, *54*, 4293–4298.
(15) Hendriksen, P. V.; Bodker, F.; Linderoth, S.; Wells, S.; Morup, S. *J. Phys. Condens. Matter* **1994**, *6*, 3081–3090.
(16) Rosensweig, R. E. *Ferrohydrodynamics*; Dover Publications: Mineola, NY, 1997; pp 103−108.
(17) Bohn, S.; Douady, S.; Courder, Y. *Phys. Rev. Lett.* **2005**, *94*, 054503-1–054503-4.
(18) Singh, K. B.; Tirumkudulu, M. S. *Phys. Rev. Lett.* **2007**, *98*, 218302-1–218302-4.
(19) NIH *Image* is a public domain image processing and analysis program for the Macintosh: http://rsb.info.nih.gov/nih-image/about.html.
(20) Skjeltorp, A. T.; Meakin, P. *Nature* **1998**, *335*, 424–426.
(21) Walmann, T.; Malthe-Sørenssen, A.; Feder, J.; Jøssang, T.; Meakin, P.; Hardy, H. H. *Phys. Rev. Lett.* **1996**, *77*, 5393–5396.

NL801501Y